Illuminating Epidermal Growth Factor Receptor Densities on Filopodia through Plasmon Coupling

Jing Wang, Svetlana V. Boriskina, Hongyun Wang, and Björn M. Reinhard*

Department of Chemistry and The Photonics Center, Boston University, Boston, Massachusetts 02215, United States

ABSTRACT Filopodia have been hypothesized to act as remote sensors of the cell environment, but many details of the sensor function remain unclear. We investigated the distribution of the epidermal growth factor (EGF) receptor (EGFR) density on filopodia and on the dorsal cell membrane of A431 human epidermoid carcinoma cells using a nanoplasmonic enabled imaging tool. We targeted cell surface EGFR with 40 nm diameter Au nanoparticles (NPs) using a high affinity multivalent labeling strategy and determined relative NP binding affinities spatially resolved through plasmon coupling. Distance-dependent near-field interactions between the labels generated a NP density (ρ)-dependent spectral response that facilitated a spatial mapping of the EGFR density distribution on subcellular length scales in an optical microscope in solution. The measured ρ values were significantly higher on filopodia than on the cellular surface, which is indicative of an enrichment of EGFR on filopodia. A detailed characterization of the spatial distribution of the NP immunolabels through scanning electron microscopy (SEM) confirmed the findings of the all-optical plasmon coupling studies and provided additional structural details. The NPs exhibited a preferential association with the sides of the filopodia. We calibrated the ρ-dependent spectral response of the Au immunolabels through correlation of optical spectroscopy and SEM. The experimental dependence of the measured plasmon resonance wavelength (λ_{res}) of the interacting immunolabels on ρ was well described by the fit $\lambda_{res} = 595.0\ \text{nm} - 46.36\ \text{nm}\ \exp(-\rho/51.48)$ for $\rho \leq 476\ \text{NPs}/\mu\text{m}^2$. The performed correlated spectroscopic/SEM studies pave the way toward quantitative immunolabeling studies of EGFR and other important cell surface receptors in an optical microscope.

KEYWORDS: epidermal growth factor receptor · filopodia · immunolabels · molecular imaging · nanoplasmonics · receptor clustering · nano–bio interface

Cell motility is a key requirement for natural growth processes, such as wound healing and embryonic development, but dysregulated cell motility enables aggressive tumor invasion in cancer.[1] Any cell translocation during normal or pathological growth requires a propelling force. The latter is generated by a branched actin network in a cytoplasmic extension—the lamellipodium—at the leading edge of moving cells.[2] Lamellipodia can contain spike-like protrusions with parallel actin bundles, which are referred to as filopodia.[3,4] A series of diverse biological functions have been attributed to filopodia, but in many cases the exact mechanisms underlying the biological function remain insufficiently characterized.[5] One proposed filopodia function is that of sensory antennae for chemotaxis in the extended environment of the cell body. In normal growth processes *in vivo*, individual cells usually need to coordinate their motility with other surrounding cells. Growth factors regulate and coordinate cell growth, and filopodia could provide information about growth factor concentrations at distant locations from the main cell body. Previous *in vitro* studies have indeed indicated a significant role for the filopodia in the "remote" sensing of the epidermal growth factor (EGF).[6,7] These studies also provided some insight into the mechanism of the sensing process and showed that, after activation through ligand binding, dimers of the EGF receptor (EGFR) were transported along the filopodia to be endocytosed at the base where the filopodia fuse with the lamellipodium.

Given the potential role of filopodia as sensor antennae, the question arises whether filopodia are equipped with a higher density (*i.e.*, number of receptors per unit area) and/or special spatial organization of EGFR that reflects this special function. Both electron microscopy[8] and fluorescent imaging techniques, such as fluorescent brightness analysis,[9,10] fluorescence resonance energy transfer (FRET) imaging,[11] and quantum dot tracking,[12] have been applied to map spatial EGFR distributions on the membranes of different cells. The work performed thus far focused, however, primarily on elucidating the receptor activation mechanism by mapping the molecular association (or clustering) of cell surface EGFR in the presence and absence of the EGF ligand and did not address the specific question of the EGFR density on filopodia.

There are some experimental indications from conventional fluorescence immunostaining studies that EGFR is enriched on microvilli, another type of actin-enriched

* Address correspondence to bmr@bu.edu.

Received for review June 3, 2011 and accepted July 17, 2011.

Published online July 17, 2011
10.1021/nn202055b

cell protrusions.[13] These studies motivated us to investigate the EGFR distribution of filopodia in more detail. To that end, we will map the spatial distribution of Au nanoparticle (NP) immunolabels selectively targeted at EGFR through a combination of electron microscopy and optical plasmon coupling microscopy (PCM). The latter utilizes the fact that—due to distance-dependent electromagnetic interactions between Au NPs[14−22]—the light scattered off NP immunolabels on the cell surface encodes direct information about the local two-dimensional NP density (ρ). The average interparticle separation between NPs decreases with increasing ρ. If ρ is high enough that the interparticle separation drops below one particle diameter, the collective coherent electron oscillations in the individual NPs—the plasmons—hybridize,[23] which induces a spectral shift in the scattering spectrum of the now coupled NP labels. Work from different groups has demonstrated that, due to the spectral shift in the spectrum of the scattered light, the near-field interactions between NP immunolabels at high ρ can be detected using conventional far-field optics.[24−28] The spectral shift in the ensemble-averaged NP resonance increases as the average interparticle separation between the NPs decreases with growing ρ.

In this article we quantify the relationship between the peak plasmon resonance wavelength (λ_{res}) and ρ for 40 nm diameter Au NP immunolabels targeted at EGFR on A431 cells. Immunolabeling strategies are commonly used to investigate receptor density distributions in the electron microscope,[8,29,30] where the spatial distribution of the NP labels is used to infer information about the local concentration of the targeted receptor. We demonstrate that the $\lambda_{res}(\rho)$ relationship enables a quantitative characterization of receptor densities on subcellular length scales through optical spectroscopy. Our plasmon coupling based approach complements conventional single NP imaging techniques[31] for localizing individual receptors in the limit of very low ρ by providing the technological means for mapping the distribution of high surface density receptors, such as EGFR, which is highly overexpressed in cancer cells.

RESULTS AND DISCUSSION

The main objective of this study is the spatial mapping of the EGFR density on different areas of the membrane. To avoid any ambiguities related to endocytosis or other cellular responses induced by NP binding, we restricted our analysis to fixed cells in this work. The visualization of the EGFR density either by optical means or SEM requires functionalized noble metal NPs that are stable against agglomeration in solution and that bind with high affinity selectively to their target. Different from conventional immunostaining studies, our combined SEM/plasmon coupling approach requires NP labels with sufficiently large scattering cross-sections to be detectable in the optical microscope.[32−34] We chose Au NPs with a nominal diameter of 40 nm and a scattering cross-section at 535 nm of $\sigma_{scat} \approx 6.05 \times 10^{-12}$ cm^2 [35] for this work. Due to their high polarizability, NPs of this size require a careful design of their surface chemistry to ensure high binding efficacy to the cell surface target and high stability against agglomeration in salt buffers at the same time. One additional complication for an efficient receptor labeling arises from the fact that epithelial cell surfaces are covered by a layer of polymeric material (glycocalyx),[36] which can impair the binding affinity of NP immunolabels to specific receptors. We performed initial labeling studies with 40 nm NPs stabilized by 3.4 kDa polyethylene glycols (PEGs), which were covalently linked to anti-EGFR antibodies. This strategy yielded, however, only NP densities of $\rho \leq 10$ NPs/μm^2 (Figure S1), which was too low for a quantification of NP binding isotherms through plasmon coupling.

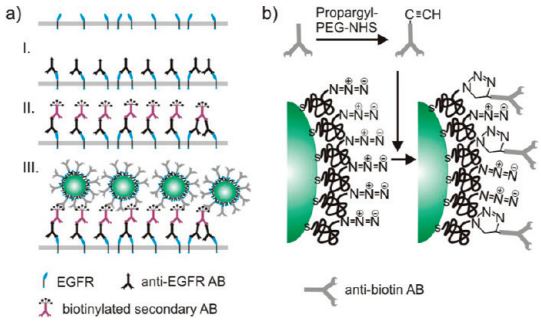

Figure 1. (a) Multivalent immunolabeling strategy of cell surface EGFR. First, primary anti-EGFR antibodies (ABs) are bound to the receptors (I). Then biotinylated secondary antibodies are anchored to the primary antibodies (II). The biotinylated antibodies carry multiple biotins to amplify the binding affinity of anti-biotin antibody functionalized Au NPs in the last step (III). (b) NP functionalization strategy through "click" chemistry. An alkyne group is introduced into the anti-biotin antibody through an amine reactive *N*-hydroxysuccinimide (NHS)-functionalized polyethylene glycol (PEG). The modified antibodies are then reacted with azide-functionalized Au NPs in a 1,3-dipolar cycloaddition.

High-Affinity EGFR Immunolabeling. In order to enhance the EGFR labeling efficiency, we designed a secondary antibody labeling strategy that amplifies the number of binding sites per EGFR on the cell surface and introduces additional structural flexibility in the attachment chemistry (Figure 1a). In the first labeling step a monoclonal anti-EGFR antibody (clone 29.1.1) is tethered to the receptors. This primary antibody is subsequently targeted by a biotinylated secondary antibody, which carries 5−8 biotin[37] molecules per antibody and thus increases the available binding sites on the cell surface. In the last step multivalent Au NPs functionalized with anti-biotin antibodies are bound to the generated biotin-binding sites. These Au immunolabels are prepared through covalent attachment of the anti-biotin antibodies to the Au NP surface using

bifunctional 3.4 kDa PEGs. The PEGs are anchored to the Au surface by a thiol residue located at one of their termini. An azide group at the second terminus of the PEGs facilitates the cross-linking with alkyne-functionalized anti-biotin antibodies using the azide−alkyne 1,3-dipolar cycloaddition "click" reaction (Figure 1b).[38] The resulting immunolabels can carry up to 80 antibodies per NP and achieve—as we will demonstrate below in more detail—high labeling efficiencies. Using these labels we achieved NP densities of up to $\rho = 476$ NPs/μm^2, which compares with $\rho \approx 10$ NPs/μm^2 for the anti-EGFR-functionalized NPs. We estimate that the secondary biotinylated antibody at which we target our gold immunolabels has a radius of gyration of approximately 6 nm.[39] The average radius of the gold nanoparticle labels is 20 nm. On the basis of steric considerations we can exclude that multiple nanoparticles binding to one secondary antibody account for the observed ~48-fold increase in NP density. Instead, we ascribe this gain to a boost in binding affinity resulting from multivalent binding interactions between the secondary antibody and the immunolabels.[40,41]

The PEGs on the NP surface have multiple important roles in our EGFR labeling strategy. They enable a covalent attachment of antibodies to the Au NP surface and, at the same time, serve as a spacer between the NP and the antibody. Due to this spacer function, the PEGs provide useful configurational flexibility for the anti-biotin antibodies, which further enhances the binding affinity. The PEGs also achieve an efficient steric stabilization[42] of the antibody-functionalized Au NPs against agglomeration in the 0.5× phosphate-buffered saline (PBS) used for the labeling studies. We monitored the UV−vis spectrum of a solution of immunolabels at a concentration of 2.9×10^{11} NPs/mL in 0.5× PBS over a time course of three hours (Figure S2). The recorded spectra did not exhibit any significant spectral shift, which confirms that the particles were stable under the chosen buffer conditions. The stability of the particles was further corroborated through a characterization of their association level through SEM. To that end, the immunolabels were first incubated in 0.5× PBS for three hours and then bound to a BSA-biotin-functionalized silicon chip for inspection in the SEM. These experiments showed that >96% of the NPs were monomers (Figure S3). Another beneficial characteristic of the sterically stabilized NPs is their low surface charge. We measured an average zeta potential of $\zeta = -7$ mV. Due to this low surface charge, the repulsion of the NPs from the negatively charged cell membrane during initial binding interactions is weak.

The nano−bio interface is complex and although the NP immunolabels are designed to bind selectively to EGFR, nonspecific interactions cannot be excluded *a priori*. It is necessary to test for nonspecific binding experimentally. Figure 2a shows a representative dark-field image of fixed A431 cells stained with 40 nm Au immunolabels (see Materials and Methods for staining details). The cells exhibit an intense green color arising from a high density of NPs bound to the cell membrane. The control in Figure 2b obtained with the same Au immunolabels but in the presence of an excess of free anti-biotin antibody in the last labeling step (step III in Figure 1a) shows no significant labeling. The anti-biotin antibody in solution binds to the biotins on the secondary antibodies and prevents the NPs from binding to the cell surface. The fact that no significant NP labeling is observed in the presence of an excess of anti-biotin antibodies proves that the nonspecific binding background is negligible.

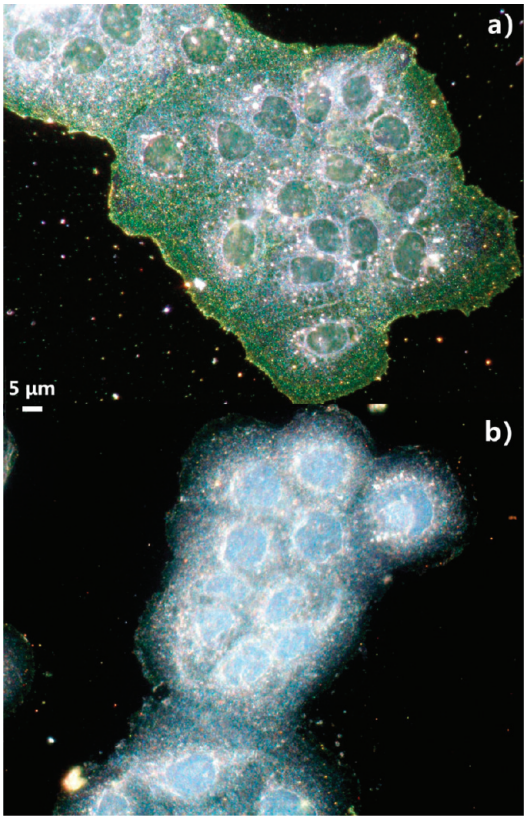

Figure 2. (a) Dark-field image of a patch of A431 cells stained for EGFR with Au immunolabels using the labeling strategy outlined in Figure 1. The bound Au NPs lead to a vivid green color on the cell surface. (b) Control experiment. The labeling procedure is identical to (a) with the exception that the cell surface was incubated with anti-biotin-functionalized Au NPs in the presence of an excess of free anti-biotin antibody in the last labeling step. The anti-biotin antibody blocks the target sites of the immunolabels and prevents specific binding.

NP Binding Isotherms Reveal Differences in ρ on Filopodia and on Cell Membranes. A magnified dark-field image of a cluster of A431 cells after labeling with Au NPs is shown in Figure 3. Filopodia extruding from two cells are clearly visible and are marked by white arrows. The peripheral membrane regions and the filopodia have low scattering backgrounds and facilitate an accurate spectroscopic characterization of bound NPs through

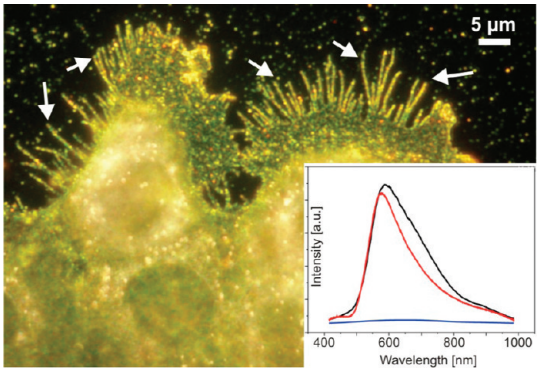

Figure 3. Magnified view of an A431 cell cluster with filopodia (marked by arrows). Inset: scattering spectra of (black) Au NP-labeled cell surface, (blue) cell background in the peripheral cell region, and (red) Au NP-labeled cell membrane spectrum after background and excitation profile correction.

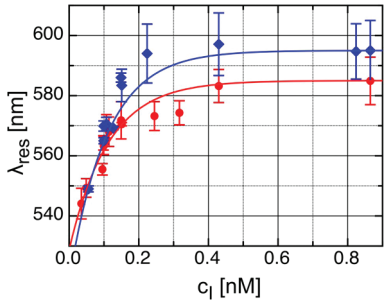

Figure 4. Resonance wavelength (λ_{res}) as function of immunolabel concentration (c_I) measured on dorsal cell membranes (red) and filopodia (blue). The observed red-shift as a function of increasing NP concentration indicates an increase in ρ. Exponential fits ($\lambda_{res} = \lambda_{max} - A \exp(-c_I/c_0)$ with the following parameters: λ_{max} = 585.0 nm; A = 56.21 nm; c_0 = 0.1124 nM (red), and λ_{max} = 595.0 nm; A = 76.57 nm; c_0 = 0.1079 nM (blue)) are included as continuous lines to guide the eye.

dark-field spectroscopy. The inset in Figure 3 contains the raw spectrum of a peripheral membrane stained by immunolabels (black), a spectrum of an unlabeled cell surface measured under identical conditions (blue), and the NP-labeled cell membrane spectrum after background and excitation profile correction (red). The scattering band associated with the NP plasmons is unambiguously detected in the spectra shown in the inset with a peak resonance wavelength at λ_{res} = 576 nm.

In the next step, we set out to record NP binding isotherms on filopodia and the cell surface by systematically measuring λ_{res} as a function of immunolabel concentration (c_I) in solution. In the case of the filopodia, we recorded scattering spectra of isolated projections and averaged λ_{res} over the entire filopodium. In the cell membrane measurements, we averaged the spectral response over an area of 2.1 μm $\times$ 50.8 μm in a peripheral region of the membrane. For each value of c_I we determined λ_{res} and the standard deviation ($\Delta\lambda_{res}$) for seven membrane measurements and at least seven filopodia on different cells. We varied c_I between 0.035 and 0.850 nM. The fixed cells were incubated with the immunolabels for 3 h at room temperature, after which the cells were washed with copious amounts of 1$\times$ PBS buffer and transferred to the dark-field microscope for spectral analysis.

The results of these experiments are summarized in Figure 4, which contains plots of $\lambda_{res}(c_I)$ for filopodia (blue) and dorsal membranes (red). Both the cell surface and the filopodia binding isotherm show initially a continuous red-shift with increasing c_I due to increased in-plane plasmon coupling[14,15] between the immunolabels as ρ increases. With increasing c_I λ_{res} does, however, not continue to increase but asymptotically approaches a maximum resonance wavelength, λ_{max}.

This saturation behavior indicates that at high NP concentrations all available binding sites on the cell surface become occupied. After the saturation conditions

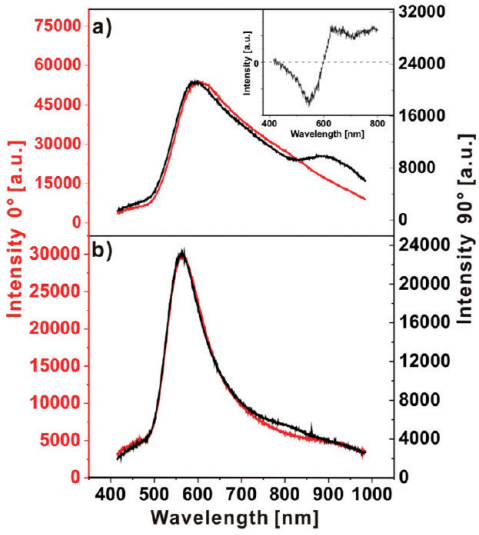

Figure 5. Scattering spectra of a single filopodium (a) and the dorsal membrane of the same cell (b) at two orthogonal analyzer angles: 0° (red) and 90° (black). In (a) the polarization directions coincide with the short (black) and long filopodium axis (red), respectively. The spectrum associated with the polarization pointing into the long filopodium axis is red-shifted relative to the spectrum with orthogonal polarization (see inset). The spectral shift is accompanied by a strong increase in scattering cross-section. The peak scattering intensity for the red spectrum is higher by 250% than for the black spectrum. In (b) two arbitrary orthogonal polarization directions are shown. The spectra for the two polarization directions superimpose, and the change in scattering intensity is small.

have been reached, a further increase in c_I no longer results in any additional binding. It is important to note that the average λ_{max} value on the filopodia is red-shifted by approximately 10 nm compared to the corresponding cell surface value (λ_{max}(filopodia) = 595 nm vs λ_{max}(surface) = 585 nm).

Since the spectral shift of λ_{res} does not increase linearly with the number of particles bound on the cell surface (see below), we refrain from an attempt to

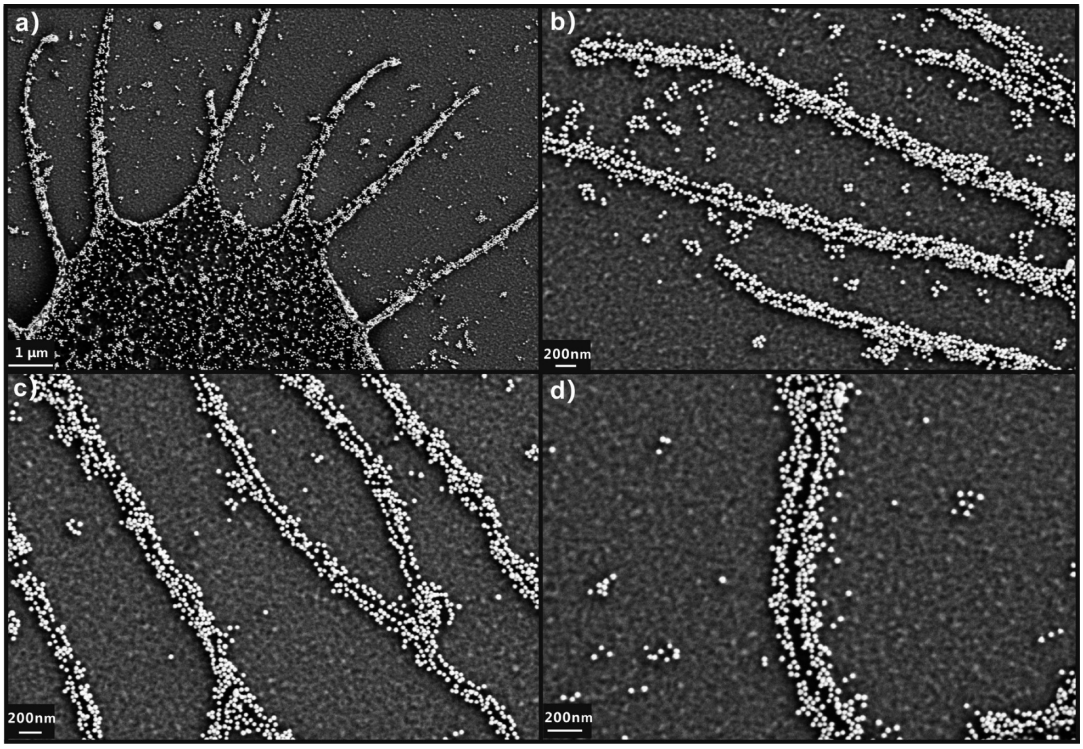

Figure 6. (a–d) SEM images of Au NP-immunolabeled cells and filopodia at different magnifications. The NP density (ρ) is higher on the filopodia than on the neighboring cell body. High-magnification SEM images (b–d) show a preferential association of the NPs with the edges of the filopodia.

determine effective binding affinities from a modeling of the change in λ_{res} as a function of c_l at this point. The observed difference in λ_{max} for the recorded binding isotherms in the asymptotic limit shows clearly that the NP binding capacity, and therefore ρ, is higher on filopodia than on the cell surface.

Polarization-Sensitive Spectral Characterization of Filopodia and Peripheral Cell Membrane Areas. To obtain additional information about the spatial organization of the NPs on cell surfaces and filopodia, we recorded polarization-resolved scattering spectra of cells that had been labeled under saturation conditions. A polarization analyzer in the beam path in front of the detector facilitated the acquisition of scattering spectra as a function of linear light polarization. Figure 5a and b show scattering spectra recorded with two orthogonal analyzer orientations on a filopodium and a peripheral area on the dorsal membrane of the same cell. In accord with an overall higher ρ on the filopodium, the peak resonance wavelength of the filopodium is red-shifted relative to that of the cell membrane (603 nm vs 567 nm). The polarization-resolved analysis of the scattering spectra reveals, however, additional instructive information. Whereas the dorsal membrane shows a polarization-independent response—the spectra for the two orthogonal light polarization directions superimpose—for the filopodium a rotation of the analyzer orientation by 90° is associated with a systematic spectral shift and change in scattering intensity. The two spectra of the filopodium in Figure 5a were obtained for polarization directions pointing along the long (red) and short (black) filopodium axis, respectively. The spectrum of the light polarized along the long filopodium axis is red-shifted (see inset in Figure 5a) by approximately 10 nm relative to the spectrum with perpendicular light polarization. This spectral red-shift is accompanied by an increase in the scattering intensity by more than 250%, which compares with a change of less than 25% for the two orthogonal polarization directions for the cell surface in Figure 5b. The spectral responses of NP clusters and assemblies are strongly morphology dependent.[43–45] The existence of spectrally distinct plasmon modes along two perpendicular axes is well known from NP clusters with high aspect ratios, such as linear chains of NPs.[46] We attribute the observed polarization properties of the light scattered off NP-labeled filopodia to the existence of such anisotropic clusters oriented with their long axes pointing into the direction of the long filopodium axis.

Mapping Immunolabel Distributions through SEM. To verify the finding from our all-optical plasmon coupling studies that ρ is higher on filopodia than on the dorsal membrane, we inspected NP-labeled cell surfaces in the SEM. To that end, the cells were immunolabeled following the same procedures used for the PCM studies and subsequently dehydrated through critical point drying (CPD) using CO_2. Since CPD avoids surface

tension in the dehydration process, it minimizes the structural perturbation during sample preparation.[47] Figure 6 contains SEM images of a cell with protruding filopodia labeled with NPs under saturation conditions. Consistent with the findings of our optical plasmon coupling studies, the SEM images show a higher local ρ on the filopodia than on the neighboring cell membrane.

The high spatial resolution of the SEM provides additional valuable information about the NP distribution on the filopodia. Although some filopodia are completely covered by NPs, more frequently we observe a preferential association of the NPs with the edges of the filopodia, where they arrange into tracks of closely coupled NPs around a core characterized by a significantly lower NP density. Due to the high contrast of the NP labels in the SEM, the low density NP cores on the filopodia are recognizable in Figure 6b–d as dark areas enclosed by bright NP-labeled filopodia edges. In areas of low ρ on the filopodia, pronounced "string-of-pearls"-like structures along the filopodia edges can be seen. The distribution of the NPs on the filopodia as observed by SEM is in agreement with the conclusions from the polarization-resolved spectral analysis, which predicted high aspect ratio NP clusters pointing along the filopodia. The higher spatial resolution of the SEM provides the additional detail that the NPs preferentially associate with the filopodia edges, which indicates a polarized distribution of EGFR on the filopodia.

A close inspection of the SEM image in Figure 6a shows that the NP density is also enriched in a thin rim located directly at the edge of the main cell body. This finding poses the question whether the observation of a higher ρ on the filopodia arises from a general edge effect due to the culturing of the cells on a two-dimensional substrate. We rule out this possibility on the basis of the observation that in many cases the high NP density on the filopodia extends further into the cell surface away from the edge (Figure 7). The observation of ordered structures of high NP density several micrometers away from the cell edge that fluently convert into the filopodia argues against a spurious edge effect as the reason for the observed high NP density. Instead, we attribute the observed structuring of the immunolabels to a patterning of EGFRs through the underlying actin network in filopodia and lamellipodium.[5] EGFR has long been known to be an actin-binding protein.[48]

SEM studies of the dorsal membrane incubated with lower NP concentrations show a measurable degree of NP clustering even at low average ρ (Figure S4). This observation is in agreement with previous studies in which we used a multispectral imaging approach to optically size NP clusters on the cell surface.[24] The current study shows now that with growing ρ—which was typically averaged over dorsal cell surface areas of approximately $13 \times 9\ \mu m^2$—the average association level and thus the sizes of the clusters increase. As we will discuss below, the preferential clustering of the NPs on the cell surface has important implications for the ρ-dependent spectral response of the immobilized NP labels.

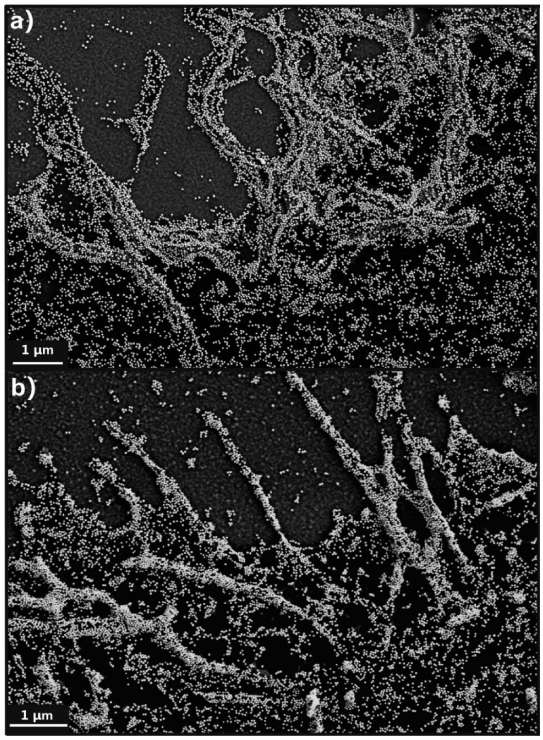

Figure 7. SEM images of Au NP-immunolabeled cell boundaries. The SEM images confirm structured areas of high NP density several micrometers away from the cell edge that fluently convert into protruding cell extensions (filopodia).

Deriving an Experimental $\lambda_{res}(\rho)$ Relationship. The consistency between our spectroscopic and SEM characterizations of the NP densities on filopodia and cell membranes confirms that the spectral mapping of plasmon coupling enables the detection of differences in ρ on subcellular length scales. Different from conventional electron microscopy, plasmon coupling microscopy requires no sample dehydration and is compatible with live cell imaging conditions. However, a determination of ρ directly from optical measurements requires a quantitative $\lambda_{res}(\rho)$ relationship that correlates the measured scattering peak wavelength with the immunolabel density on the cell surface. We set out to experimentally determine such a relationship in the investigated system by measuring λ_{res} and ρ on A431 cells after incubation with different NP concentrations for 3 h. Figure 8 contains the obtained $\lambda_{res}(\rho)$ plot. To span the largest possible ρ-range we included data points measured both on the cell surface (green squares) and on filopodia (blue diamonds). We find that the $\lambda_{res}(\rho)$ relationship is well described by an exponential saturation growth model: $\lambda_{res}(\rho) = [595.0 - 46.36\ \exp(-\rho/51.48)]$ nm (continuous red line in Figure 8). The experimentally derived $\lambda_{res}(\rho)$

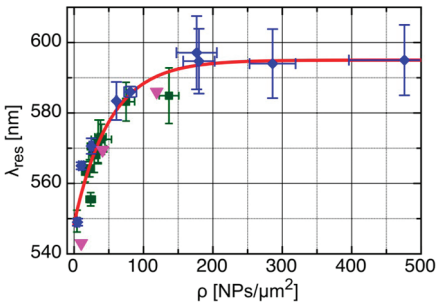

Figure 8. Plasmon resonance wavelength (λ_{res}) *vs* NP density (ρ) on the cell membrane and protruding filopodia of A431 cells. Cell surface measurements are plotted as green squares; filopodia measurements, as blue diamonds. An exponential fit ($\lambda_{res} = \lambda_{max} - A \exp(-\rho/\rho_0)$) with the parameters λ_{max} = 595.0 nm, A = 46.36 nm, and ρ_0 = 51.48 NPs/μm^2 is included as a red continuous line. Pink triangles correspond to simulated peak wavelengths using generalized multiparticle Mie theory.

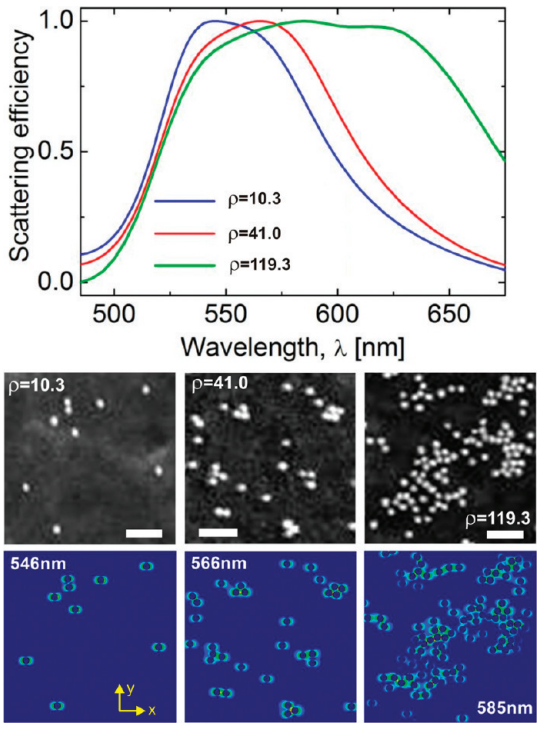

Figure 9. Simulated near- and far-field responses of experimentally observed NP distributions. The Rayleigh scattering spectra (top) were simulated assuming the NP distributions with different ρ values shown in the middle row. The bottom row contains the calculated E-field intensity distributions at the given wavelengths (the excitation light is polarized along the *x*-axis). All size bars are 200 nm.

relationship paves the way toward determining NP densities up to ρ = 200 NPs/μm^2 based entirely on spectral information. An increase of ρ beyond 200 NPs/μm^2 does not lead to a further increase in λ_{res}, so that the discrimination of even higher NP densities still requires an inspection in the electron microscope. We emphasize, however, that the dynamic range of 0−200 NPs/μm^2 for spectroscopic ρ measurements will be sufficient for most practical applications, such as monitoring EGFR overexpression.

To elucidate the underlying electromagnetic interaction mechanisms between the NPs on the cell surface in more detail, we simulated the spectral response of different experimentally observed spatial NP distributions through generalized multiparticle Mie simulations. In Figure 9 we show simulated far-field scattering spectra for three experimentally observed NP distributions (middle row) with NP densities of ρ = 10.3−119.3 NPs/μm^2. The simulated scattering spectra show a gradual red-shift and broadening as ρ increases. The λ_{res} values corresponding to the peak scattering intensities in the simulated spectra are included in Figure 8 as pink triangles and reproduce the experimental $\lambda_{res}(\rho)$ relationship remarkably well.

The spatial distribution of the E-field intensities for the investigated NP distributions shown in the bottom row in Figure 9 provides further valuable insight in the observed $\lambda_{res}(\rho)$ dependence. At low ρ (ρ = 10.3 NPs/μm^2) the spectral response is dominated by individual, noninteracting NPs on the cell surface. Although even at these low ρ values some clusters are already present, the number of individual NPs is higher and the resonance wavelength of the ensemble average is determined by the noninteracting NPs. Since in the case of EGFR the immunolabels have a high propensity to cluster on the cell surface, the number of clusters sharply increases at medium ρ values (as shown here for ρ = 41.0 NPs/μm^2). In the clusters the plasmons of the individual NPs couple, which results in a spectral red-shift of the resonance wavelength with regard to that of individual, well-separated NPs.[43,49] Consequently, if present in substantial quantities, clusters red-shift the ensemble-averaged spectrum of the NP labels. We attribute the fact that we observe significant clustering already at low to medium ρ values to a heterogeneous distribution of EGFR on the cell surface and its concentration in special microdomains.

With growing ρ the average cluster size of the NP immunolabels on the cell surface increases and the ensemble-averaged spectral response further red-shifts and broadens as shown for ρ = 119.3 NPs/μm^2. The simulated E-field intensity distributions for ρ = 41.0 and 119.3 NPs/μm^2 illustrate that plasmon coupling on the cell surface is dominated by nearest neighbor interactions. Consequently, the magnitude of the spectral shift decreases as the cluster sizes grow even further for ρ > 119.3. Figure 8 shows that, at very high ρ, λ_{res} becomes almost independent of the nanoparticle density. This effect was observed before with nanofabricated NP clusters of defined size.[49]

CONCLUSIONS

Using a multivalent labeling strategy we achieved a highly efficient and selective labeling of EGFR on A431 human epidermoid carcinoma cells with 40 nm Au NPs. We demonstrated experimentally through a

combination of optical spectroscopy and electron microscopy as well as through computational electromagnetics that the distance-dependent near-field interactions between NP immunolabels enable characterizing the average NP density (ρ) on the cell surface on subcellular length scales. We utilized the ρ dependence of the collective spectral response to monitor spatially resolved NP binding isotherms in an optical microscope. We found that under saturation conditions ρ is significantly higher on filopodia than on the remaining cell surface, which indicates a higher EGFR density on filopodia. Our observation of an EGFR enrichment on filopodia is consistent with an important sensory function for filopodia. The high local EGFR concentration in combination with their ability to provide sensory information at large separations from the cell body makes filopodia uniquely suited for remote EGF sensing and thus for providing cancer cells with the sensory input required for directed motility.

The correlation of λ_{res} and ρ enables other important applications besides characterizing the EGFR density on filopodia. Overexpression of EGFR enhances the motility of cancer cells *in vivo*[50] and is thus correlated with a poor prognosis.[51,52] The cell surface concentration of EGFR, in particular, is thought to encode important information about the molecular nature of a tumor.[53−55] Given the relevance of EGFR concentrations and distributions for cancer diagnostics, the $\lambda_{res}(\rho)$ relationship derived in this work provides important new opportunities for cancer detection and staging modalities by enabling a quantitative optical mapping of EGFR immunolabel densities. Similar analyses to those performed for EGFR in this work will in the future be possible with different receptors. We emphasize that the exact form of the $\lambda(\rho)$ relationship will depend on the spatial organization of the receptors on subdiffraction limit length scales. In the case of the EGFR the immunolabels were found to cluster on the cell surface even at low to medium NP densities, which is consistent with a heterogeneous receptor distribution. Generalized multiple-particle Mie scattering simulations of experimentally observed NP distributions as a function of ρ reproduced the experimental $\lambda_{res}(\rho)$ dependence and confirmed that the ρ-dependence of the collective spectral response is dominated by nearest neighbor interactions in immunolabel clusters.

MATERIALS AND METHODS

Materials. The following materials were used as obtained from the vendors: 40 nm Au colloid (Ted Pella); thiol-polyethylene glycol-azide (N_3-$(CH_2CH_2O)_{77}$-CH_2CH_2−SH, molecular weight 3400) (NANOCS); propargyl dPEG-NHS ester (Quanta Biodesign); monoclonal anti-epidermal growth factor receptor antibody (29.1) (Sigma); anti-biotin affinity isolated antigen specific antibody (Sigma); anti-mouse IgG biotin conjugate (Sigma); L-ascorbic acid (Aldrich); copper(II) sulfate pentahydrate (Aldrich). We used ZebaTM spin desalting columns (7K MWCO) from Thermo Scientific.

Particle Functionalization. Thiol-polyethylene glycol-azide (thiol-PEG-azide) was used for surface modification of 40 nm AuNPs. The thiol-PEG-azide solution (10 mM, 5 μL) was incubated with AuNPs (~9×10^{10} particles/mL) overnight at room temperature. After that, the PEG-modified AuNPs were washed three times by centrifugation (5.500 rpm, 10 min) and resuspension in distilled deionized (ddi) water. The volume of the Au NP solution after the final washing step was 20 μL. A 2 μL amount of a solution of propargyl-PEG-NHS ester (100 mg/mL dissolved in DMSO) was mixed with 100 μL of a 1 mg/mL anti-biotin antibody solution in 1× PBS, pH 7.2, in an ice bath for 6 h. After that the excess propargyl-PEG-NHS ester was removed using a size exclusion column (7K MWCO). A 100 μL amount of the propargyl-PEG-anti-biotin antibody was then incubated with 20 μL of the PEG-modified AuNPs in the presence of a click chemistry catalyst (100 nmol of ascorbic acid and 20 nmol of $CuSO_4$) overnight at 4 °C. The resulting immunolabels were washed three times by centrifugation (4.500 rpm, 10 min) and resuspension in water. After the final centrifugation step, the cleaned immunolabels were resuspended in 0.5× PBS, pH 7.2.

Cell Culture. A431 cells were cultured in Dulbecco's modified Eagle's medium (DMEM) supplemented with L-glutamine, penicillin, and streptomycin in a 5% CO_2 containing atmosphere with 95% relative humidity in an incubator at 37 °C. Cells to be immunolabeled and imaged by dark-field microscopy were grown on glass coverslips to approximately 30% confluency. The cells used for SEM studies were grown on 1 × 1 cm silicon substrates.

Immunolabeling and Sample Preparation for Optical Studies. A431 cells were fixed by immersion in a 4% formaldehyde solution for 10 min at room temperature. The cells were then washed three times by immersion into ice-cold 1× PBS for 5 min each time. The fixed cells were then incubated in ice-cold 1× PBS buffer containing 1% BSA for 1 h at room temperature to block nonspecific binding. After that the cells were washed again three times with ice-cold 1× PBS for 5 min each. The cell slides were then incubated with monoclonal anti-EGFR antibody (diluted 1:100 in 1× PBS) at 4 °C overnight. The cells were subsequently washed three times with ice-cold 1× PBS for 5 min each. After that, biotin-labeled secondary IgG antibody (diluted 1:100 in 1× PBS) was incubated with the above cell slides for 1 h at room temperature. Then the cells were again washed three times with ice-cold 1× PBS for 5 min each. In the subsequent immunolabeling step, each cell slide was covered with 200 μL of propargyl-PEG-anti-biotin linked Au NPs for 3 h at room temperature in a water vapor saturated atmosphere and then washed with ice-cold 1× PBS three times for 5 min. The cell slides were then integrated into a homemade flow chamber and transferred to a dark-field microscope for optical inspection.

Preparation of SEM Samples. The culture and immunolabeling procedures were identical to sample preparation for the optical studies with the exception that the A431 cells were grown on silicon substrates. After immunolabeling, the silicon substrates were washed twice with ice-cold 1× PBS and then briefly immersed into ddi water to remove the salt on the surface. Right before imaging in the SEM, the silicon substrates were washed three times with 95% ethanol at −20 °C and then dried using a CO_2 critical point dryer (SPI Supplies Structure Probe, Inc.).

Dark-Field Microscopy. We used a fixed-stage Olympus BX51W1 microscope with a high numerical aperture (NA) oil condenser (NA = 1.2−1.4) and a 60× oil objective (NA = 0.65). Color images were recorded on an Olympus SP310 digital camera attached to the microscope through an eyepiece

adapter. The samples were illuminated with a 100 W xenon lamp (for all spectroscopic studies) or with a 100 W tungsten lamp.

Dark-Field Spectroscopy. Scattering spectra were recorded using a 303 mm imaging spectrometer (Andor Shamrock 303i) attached to the microscope. We used a 150 lines/mm grating with a blaze wavelength at 500 nm and collected the dispersed light using a back-illuminated CCD camera (Andor DU 401-BR-DD). The adjustable opening slit of the spectrometer facilitates a spatial filtering of the detected light. The opening of the slit was used to confine the area of interest along one dimension; the second dimension (the height of the captured image on the CCD) was controlled through the software. The adjustable slit and a rotational sample mount enabled measuring spectra from the cell surface as well as from individual filopodia. The cell surface spectra were background corrected by subtraction of the average scattering spectrum of an unlabeled cell surface of identical size (average of seven spectra) and corrected for the excitation profile of the xenon white light by dividing through the spectrum of an ideal white light scatterer. Filopodia spectra were background corrected with an average background spectrum obtained from seven individual, unlabeled filopodia. The white light correction was identical to the procedures described for the cell surface spectra.

Zeta-Potential Measurements. Zeta-potential measurements of NP immunolabels in 0.5× PBS were performed using a Malvern NANO-ZS90 Zetasizer at 25 °C.

Computational Electromagnetics. Far-field scattering spectra and near-field intensity distributions were calculated with generalized multiparticle Mie theory (GMT), which provides an exact analytical solution of Maxwell's equations for an arbitrary configuration of L spheres.[56,57] In this approach the electromagnetic field is constructed as a superposition of partial fields scattered by each sphere expanded in the orthogonal basis of vector spherical harmonics: $E^l_{sc} = \Sigma_{(n)}\,\Sigma_{(m)}\,(a^l_{mn}\mathbf{N}_{mn} + b^l_{mn}\mathbf{M}_{mn})$, $l = 1, ..., L$. A matrix equation for the Lorenz−Mie multipole scattering coefficients (a^l_{mn}, b^l_{mn}) is obtained by imposing the field continuity conditions on the particle surfaces, using the translation theorem for vector spherical harmonics and truncating the infinite series expansions to a maximum multipolar order N. In the calculations performed in this work the NPs were excited by a plane wave with an angle of incidence of 54° to normal to account for the oblique illumination angle in dark-field microscopy. The calculated scattering efficiencies were polarization-averaged and normalized to unity. For the nanospheres we used the refractive index values from Johnson and Christy.[58] Our GMT code is restricted to applications in homogeneous media. We therefore used an effective medium approximation[59] to account for the interface between the cell surface and the aqueous environment. In the simulations the particles were immersed in an ambient medium with an effective refractive index of $n_r = 1.39$, which was calculated as an average of the refractive indices of the membrane ($n_r = 1.45$) and the surrounding water ($n_r = 1.33$).

Acknowledgment. This work was supported by the National Institutes of Health (NIH/NCI) through grant 5R01CA138509-03.

Supporting Information Available: Figures S1−S4. This material is available free of charge *via* the Internet at http://pubs.acs.org.

REFERENCES AND NOTES

1. Kassis, J.; Lauffenburger, D. A.; Turner, T.; Wells, A. Tumor Invasion as Dysregulated Cell Motility. *Semin. Cancer Biol.* **2001**, *11*, 105–117.
2. Lauffenburger, D. A.; Horwitz, A. F. Cell Migration: A Physically Integrated Molecular Process. *Cell* **1996**, *84*, 359–369.
3. Faix, J.; Rottner, K. The Making of Filopodia. *Curr. Opin. Cell Biol.* **2006**, *18*, 18–25.
4. Mejlillano, M. R.; Kojima, S.; Applewhite, D. A.; Gertler, F. B.; Svitkina, T. M.; Borisy, G. G. Lamellipodial Versus Filopodial Mode of the Actin Nanomachinery: Pivotal Role of the Filament Barbed End. *Cell* **2004**, *118*, 363–373.
5. Matilla, P. K.; Lappalainen, P. Filipodia: Molecular Architecture and Cellular Function. *Nat. Rev. Mol. Cell Biol.* **2008**, *9*, 446–454.
6. Lidke, D. S.; Lidke, K. A.; Rieger, B.; Jovin, T. M.; Arndt-Jovin, D. J. Reaching Out for Signals: Filopodia Sense EGF and Respond by Directed Retrograde Transport of Activated Receptors. *J. Cell Biol.* **2005**, *170*, 619–626.
7. Lidke, D. S.; Nagy, P.; Heintzmann, R.; Arndt-Jovin, D. J.; Post, J. N.; Grecco, H. E.; Jares-Erijman, E. A.; Jobin, T. M. Quantum Dot Ligands Provide New Insights into ErbB/HER Receptor Mediated Signal Transduction. *Nat. Biotechnol.* **2004**, *22*, 198–203.
8. Yang, S.; Raymond-Stintz, M. A.; Ying, W.; Zhang, J.; Lidke, D. S.; Steinberg, S. L.; Williams, L.; Oliver, J. M.; Wilson, B. S. Mapping ErbB Receptors on Breast Cancer Cell Membranes during Signal Transduction. *J. Cell Sci.* **2007**, *120*, 2763–2773.
9. Nagy, P.; Claus, J.; Jovin, T. M.; Arndt-Jovin, D. J. Distribution of Resting and Ligand-Bound ErbB1 and ErbB2 Tyrosine Kinases in Living Cells Using Number and Brightness Analysis. *Proc. Natl. Acad. Sci. U. S. A.* **2010**, *107*, 16524–16529.
10. Saffarian, S.; Li, Y.; Elson, E. L.; Pike, L. J. Oligomerization of the EGF Receptor Investigated by Live Cell Fluorescence Intensity Distribution Analysis. *Biophys. J.* **2007**, *93*, 1021–1031.
11. Bader, A. N.; Hofman, E. G.; Voortman, J.; van Bergen en Henegouwden, P. M. P.; Gerritsen, H. C. Homo-FRET Imaging Enables Quantification of Protein Cluster Sizes with Subcellular Resolution. *Biophys. J.* **2009**, *97*, 2613–2622.
12. Chung, I.; Akita, R.; Vandlen, R.; Toomre, D.; Schlessinger, J.; Mellman, I. Spatial Control of EGF Receptor Activation by Reversible Dimerization on Living Cells. *Nature* **2010**, *464*, 783–787.
13. Lichtner, R. B.; Schirrmacher, V. Cellular Distribution and Biological Activity of Epidermal Growth Factor Receptors in A431 Cells Are Influenced by Cell-Cell Contact. *J. Cell. Physiol.* **1990**, *144*, 303–312.
14. Reinhard, B. M.; Siu, M.; Agarwal, H.; Alivisatos, A. P.; Liphardt, J. Calibration of Dynamic Molecular Rule Based on Plasmon Coupling between Gold Nanoparticles. *Nano Lett.* **2005**, *5*, 2246–2252.
15. Yang, L.; Wang, H.; Yan, B.; Reinhard, B. M. Calibration of Silver Plasmon Rulers in the 1−25 nm Separation Range: Experimental Indications of Distinct Plasmon Coupling Regimes. *J. Phys. Chem. C* **2010**, *114*, 4901–4908.
16. Wei, Q. H.; Su, K. H.; Durant, S.; Zhang, X. Plasmon Resonance of Finite One-Dimensional Au Nanoparticle Chains. *Nano Lett.* **2004**, *4*, 1067–1071.
17. Jain, P. K.; Huang, W. Y.; El-Sayed, M. A. On the Universal Scaling Behavior of the Distance Decay of Plasmon Coupling in Metal Nanoparticle Pairs: A Plasmon Ruler Equation. *Nano Lett.* **2007**, *7*, 2080–2088.
18. Rechberger, W.; Hohenau, A.; Leitner, A.; Krenn, J. R.; Lamprecht, B.; Aussenegg, F. R. Optical Properties of Two Interacting Gold Nanoparticles. *Opt. Commun.* **2003**, *220*, 137–141.
19. Elghanian, R.; Storhoff, J. J.; Mucic, R. C.; Letsinger, R. L.; Mirkin, C. A. Selective Colorimetric Detection of Polynucleotides Based on the Distance-Dependent Optical Properties of Gold Nanoparticles. *Science* **1997**, *277*, 1078–1081.
20. Gunnarsson, L.; Rindzevicius, T.; Prikulis, J.; Kasemo, B.; Kall, M. Confined Plasmons in Nanofabricated Single Silver Particle Pairs: Experimental Observations of Strong Interparticle Interactions. *J. Phys. Chem. B* **2005**, *109*, 1079–1087.
21. Lassiter, J. B.; Aizpurua, J.; Hernandez, L. I.; Brandl, D. W.; Romero, I.; Lal, S.; Hafner, J. H.; Nordlander, P.; Halas, N. J. Close Encounters between Two Nanoshells. *Nano Lett.* **2008**, *8*, 1212–1218.
22. Atay, T.; Song, J. H.; Nurmikko, A. V. Strongly Interacting Plasmon Nanoparticle Pairs: From Dipole−Dipole Interaction to Conductively Coupled Regime. *Nano Lett.* **2004**, *4*, 1627–1631.
23. Nordlander, P.; Oubre, C.; Prodan, E.; Li, K.; Stockman, M. I. Plasmon Hybridization in Nanoparticle Dimers. *Nano Lett.* **2004**, *4*, 899–903.

24. Wang, H.; Rong, G; Yan, B.; Reinhard, B. M. Optical Sizing of Immunolabel Clusters through Multispectral Plasmon Coupling Microscopy. *Nano Lett.* **2011**, *11*, 498–504.
25. Aaron, J.; Travis, K.; Harrison, N.; Sokolov, K. Dynamic Imaging of Molecular Assemblies in Live Cells Based on Nanoparticle Plasmon Resonance Coupling. *Nano Lett.* **2009**, *9*, 3612–3618.
26. Aaron, J.; Nitin, N.; Travis, K.; Kumar, S.; Collier, T.; Park, S. Y.; José-Yacamán, M.; Coghlan, L.; Follen, M.; Richards-Kortum, R.; *et al*. Plasmon Resonance Coupling of Metal Nanoparticles for Molecular Imaging of Carcinogenesis *in Vivo*. *J. Biomed. Opt.* **2007**, *12*, 034007.
27. Crow, M. J.; Grant, G.; Provenzale, J. M.; Wax, A. Molecular Imaging and Quantitative Measurement of Epidermal Growth Factor Receptor Expression in Live Cancer Cells Using Immunolabeled Gold Nanoparticles. *Am. J. Roentgenol.* **2009**, *192*, 1021–1028.
28. Qian, W.; Huang, X.; Kang, B.; El-Sayed, M. A. Dark-field Light Scattering Imaging of Living Cancer Cell Component from Birth through Division Using Bioconjugated Gold Nanoprobes. *J. Biomed. Opt.* **2010**, *15*, 046025.
29. Lessard, A.; Coleman, C. G.; Pickel, V. M. Chronic Intermittent Hypoxia Reduces Neurokinin-1 (NK_1) Receptor Density in Small Dendrites of Non-catecholaminergic Neurons in Mouse Nucleus Tractus Solitarius. *Exp. Neurol.* **2010**, *223*, 634–644.
30. Stump, R. F.; Pfeiffer, J. R.; Seagrave, J.; Oliver, J. M. Mapping Gold-labeled IgE Receptors on Mast Cells by Scanning Electron Microscopy: Receptor Distributions Revealed by Silver Enhancement, Backscattered Electron Imaging, and Digital Image Analysis. *J. Histochem. Cytochem.* **1988**, *36*, 493–503.
31. Huang, T.; Nallathamby, P. D.; Gillet, D.; Xu, X-H. N. Design and Synthesis of Single-Nanoparticle Optical Biosensors for Imaging and Characterization of Single Receptor Molecules on Single Living Cells. *Anal. Chem.* **2007**, *79*, 7708–7718.
32. Sonnichsen, C.; Franzl, T.; Wilk, T.; von Plessen, G.; Feldmann, J. Plasmon Resonances in Large Noble-Metal Clusters. *New J. Phys.* **2002**, *4*, 93.1–93.8.
33. Schultz, S.; Smith, D. R.; Mock, J. J.; Schultz, D. A. Single-target Molecule Detection with Nonbleaching Multicolor Optical Immunolabels. *Proc. Natl. Acad. Sci. U. S. A.* **2000**, *97*, 996–1001.
34. Murphy, C. J.; Gole, A. M.; Stone, J. W.; Sisco, P. N.; Alkilany, A. M.; Goldsmith, E. C.; Baxter, S. C. Gold Nanoparticles in Biology: Beyond Toxicity to Cellular Imaging. *Acc. Chem. Res.* **2008**, *41*, 1721–1730.
35. Yguerabide, J.; Yguerabide, E. E. Light-Scattering Submicroscopic Particles as Highly Fluorescent Analogs and Their Use as Tracer Labels in Clinical and Biological Applications - I. Theory. *Anal. Biochem.* **1998**, *262*, 137–156.
36. Turoverova, L. V.; Khotin, M. G.; Yudintseva, N. M.; Magnusson, K. E.; Blinova, M. I.; Pinaev, G. P.; Tentler, D. G. Analysis of Extracellular Matrix Proteins Produced by Cultured Cells. *Cell Tissue Biol.* **2009**, *3*, 497–502.
37. Der-Balian, G. P.; Gomez, B.; Masino, R. S.; Parce, J. W. A Fluorimetric Method for Determining the Degree of Biotinylation of Proteins. *J. Immunol. Methods* **1990**, *126*, 281–285.
38. Kolb, H. C.; Finn, M. G.; Sharpless, K. B. Click Chemistry: Diverse Chemical Function from a Few Good Reactions. *Angew. Chem., Int. Ed.* **2001**, *40*, 2004–2021.
39. Cser, L.; Gladkib, I. A.; Franek, F.; Ostanevich, Y. M. Investigation of Antibody Structures by Scattering Techniques. *Colloid Polym. Sci.* **1981**, *259*, 625–640.
40. Bowman, M. C.; Ballard, T. E.; Ackerson, C. J.; Feldheim, D. L.; Margolis, D. M.; Melander, C. Inhibition of HIV Fusion with Multivalent Gold Nanoparticles. *J. Am. Chem. Soc.* **2008**, *130*, 6898–6897.
41. Lytton-Jean, A. K. R.; Mirkin, C. A. A Thermodynamic Ivestigation into the Binding Properties of DNA Functionalized Gold Nanoparticle Probes and Molecular Fluorophore Probes. *J. Am. Chem. Soc.* **2005**, *127*, 12754–12755.
42. Napper, D. H. *Polymeric Stabilization of Colloidal Dispersions*; Academic Press: London, 1983.
43. Yan, B.; Boriskina, S. V.; Reinhard, B. M. Optimizing Gold Nanoparticle Cluster Configurations ($n \leq 7$) for Array Applications. *J. Phys. Chem. C* **2011**, *115*, 4578–4583.
44. Wang, H.; Brandl, D. W.; Nordlander, P.; Halas, N. J. Plasmonic Nanostructures: Artificial Molecules. *Acc. Chem. Res.* **2007**, *40*, 53–62.
45. Brandl, D. W.; Mirin, N. A.; Nordlander, P. Plasmon Modes of Nanosphere Trimers and Quadrumers. *J. Phys. Chem. B* **2006**, *110*, 12302–12310.
46. Maier, S. A.; Brongersma, M. L.; Kik, P. G.; Atwater, H. A. Observation of Near-field Coupling in Metal Nanoparticle Chains Using Far-Field Polarization Spectroscopy. *Phys. Rev. B* **2002**, *65*, 193408.
47. Schliwa, M. The Evolving Complexity of Cytoplasmic Structure. *Nat. Rev. Mol. Cell Biol.* **2002**, *3*, 291–295.
48. den Hartigh, J. C.; van Bergen en Henegouwen, P. M. P.; Verkleij, A. J.; Boonstra, J. The EGF Receptor is an Actin-binding Protein. *J. Cell Biol.* **1992**, *119*, 349–355.
49. Yan, B.; Thubagere, A.; Premasiri, W. R.; Ziegler, L. D.; Dal Negro, L.; Reinhard, B. M. Engineered SERS Substrates with Multiscale Signal Enhancement: Nanoparticle Cluster Arrays. *ACS Nano* **2009**, *3*, 1190–1202.
50. Xue, C.; Wyckoff, J.; Liang, F.; Sidani, M.; Violini, S.; Tsai, K.; Zhang, Z.; Sahai, E.; Condeelis, J.; Segall, J. E. Epidermal Growth Factor Receptor Overexpression Results in Increased Tumor Cell Motility *in Vivo* Coordinately with Enhanced Intravasation and Metastasis. *Cancer Res.* **2006**, *66*, 192–197.
51. Nicholson, R. I.; Gee, J. M. W.; Harper, M. E. EGFR and Cancer Prognosis. *Eur. J. Cancer* **2001**, *37*, S9–S15.
52. Sibilia, M.; Kroismayr, R.; Lichtenberger, B. M.; Natarajan, A.; Hecking, M.; Holcmann, M. The Epidermal Growth Factor Receptor: From Development to Tumorigenesis. *Differentiation* **2007**, *75*, 770–787.
53. Thiery, J. P. Epithelial-mesenchymal Transitions in Tumour Progression. *Nat. Rev. Cancer* **2002**, *2*, 442–454.
54. de Graauw, M.; van Miltenburg, M. H.; Schmidt, M. K.; Pont, C.; Lalai, R.; Kartopawiro, J.; Pardali, E.; Le Dévédec, S. E.; Smit, V. T.; van der Wal, A.; *et al*. Annexin A1 Regulates TGF-b Signaling and Promotes Metastasis Formation of Basal-like Breast Cancer Cell. *Proc. Natl. Acad. Sci. U. S. A.* **2010**, *107*, 6340–6345.
55. Burel-Vandenbos, F.; Benchetrit, M.; Miquel, C.; Fontaine, D.; Auvergne, R.; Lebrun-Frenay, C.; Cardot-Leccia, N.; Michiels, J. F.; Paquis-Flucklinger, V.; Virolle, T. EGFR Immunolabeling Pattern May Discriminate Low-Grade Gliomas from Gliosis. *J. Neuro-Oncol.* **2011**, *102*, 171–178.
56. Xu, Y. L. Electromagnetic Scattering by an Aggregate of Spheres. *Appl. Opt.* **1995**, *34*, 4573–4588.
57. Gopinath, A.; Boriskina, S. V.; Feng, N. N.; Reinhard, B. M.; Dal Negro, L. Photonic-plasmonic Scattering Resonances in Deterministic Aperiodic Structures. *Nano Lett.* **2008**, *8*, 2423–2431.
58. Johnson, P. B.; Christy, R. W. Optical Constants of the Noble Metals. *Phys. Rev. B* **1972**, *6*, 4370–4379.
59. Tamaru, H.; Kuwata, H.; Miyazaki, H. T.; Miyano, K. Resonant Light Scattering from Individual Ag Nanoparticles and Particle Pairs. *Appl. Phys. Lett.* **2002**, *80*, 1826–1828.